Chinese Journal of Aeronautics, (2018), 31(9): 1870–1879

Chinese Society of Aeronautics and Astronautics
& Beihang University

Chinese Journal of Aeronautics

cja@buaa.edu.cn
www.sciencedirect.com

Numerical studies on supersonic spray combustion in high-temperature shear flows in a scramjet combustor

Zhaoxin REN [a], **Bing WANG** [b,*], **Longxi ZHENG** [a], **Dan ZHAO** [c]

[a] *School of Power and Energy, Northwestern Polytechnical University, Xi'an 710072, China*
[b] *School of Aerospace Engineering, Tsinghua University, Beijing 100084, China*
[c] *Department of Mechanical Engineering, College of Engineering, University of Canterbury, Private Bag 4800, Christchurch 8140, New Zealand*

Received 24 January 2018; revised 12 March 2018; accepted 15 April 2018
Available online 05 July 2018

KEYWORDS

Combustion;
Flame kernel;
Mixing layer;
Numerical simulation;
Shearing vortex;
Spray flame;
Supersonic flow

Abstract Numerical simulation is applied to detail the combustion characteristics of n-decane sprays in highly compressible vortices formed in a supersonic mixing layer. The multi-phase reacting flow is modeled, in which the shear flow is solved Eulerianly by means of direct numerical simulation, and the motions of individual sub-grid point-mass fuel droplets are tracked Lagrangianly. Spray combustion behaviors are studied under different ambient pressures. Results indicate that ignition kernels are formed at high-strain vortex braids, where the scalar dissipation rates are high. The flame kernels are then strongly strained, associated with the rotation of the shearing vortex, and propagate to envelop the local vortex. It is observed that the flammable mixtures entrained in the vortex are burned from the edge to the core of the vortex until the reactants are completely consumed. As the ambient pressure increases, the high-temperature region expands so that the behaviors of spray flames are strongly changed. An overall analysis of the combustion field indicates that the time-averaged temperature increases, and the fluctuating pressure decreases, resulting in a more stable spray combustion under higher pressures, primarily due to the acceleration of the chemical reaction.

1. Introduction

A comprehensive understanding of the physics of spray flames associated with the vortex dynamics in highly compressible flows is desired for the optimal design and operation of scramjet combustors. The high airstream velocity and hence the flow compressibility inside a combustor reduce the residence time

* Corresponding author.
E-mail address: wbing@tsinghua.edu.cn (B. WANG).
Peer review under responsibility of Editorial Committee of CJA.

ELSEVIER Production and hosting by Elsevier

https://doi.org/10.1016/j.cja.2018.06.020

available for evaporation of atomized droplets, fuel-oxidizer mixing, and combustion, and also preclude flame propagation. A stable combustion must depend on auto-ignition due to high-speed flow velocities, and ignition and flame propagation are usually influenced by the unsteady motions of turbulent eddies.

Most available literature concentrated on low-speed/subsonic combustion of fuel sprays[1–13]. Miller[1] investigated the influence of reacting/non-reacting fuel droplets/particles on combustion characteristics in a compressible shear flow via numerical simulations. Reveillon and Vervisch[3] numerically studied the flame structures of spray combustion and considered the effects of the equivalence ratio and dilution. Supersonic combustion has been investigated through experiments subjected to some certain conditions, but there is a lack of flow-field data due to the limitation of experimental measurement technology[4–8]. Stable combustion in supersonic flows pertains to thermal auto-ignition of flammable mixtures and flame anchoring by cavities or struts[4]. The influence of the combustor pressure on supersonic combustion has not been well studied, which can accelerate the chemical reaction and increase the heat release intensity. In addition, such effects should be associated with the vortex dynamics during spray combustion, since fuel droplets will be dispersed by the motions of vortices in the flow field.

The droplet size and equivalence ratio have influences on spray combustion characteristics. Previous research has shown that droplets change flame structures, in which a diffusion-like combustion occurs for large droplets due to a slow evaporation process, while a premixed-like combustion is evident[9] for small droplets. This is mainly because the ignition process of spay fuels is found to be mixing-controlled for small-sized droplets, but evaporation-controlled for large-sized droplets[13]. Later studies have found that the gaseous temperature is suppressed by the increase of the droplet mass flow rate due to the thermal cooling effect from droplet evaporation[9]. However, those studies were initiated from low-speed flows, and spray combustion in high-speed flows will be influenced by the high-speed flow compressibility. The compressibility will depress the large vortex spatiotemporal evolution. Large vortices coexist with small vortices in a supersonic flow field. Although small eddies could also influence the mixing process as well as the chemical reaction, it should be noted that their effects on combustion features are less obvious than those of large eddies[4]. Therefore, the influences of the turbulent motions of large eddies on auto-ignition and flame propagation should be studied considering the high-compressibility effects.

The aim of the present investigation is to study spray flames associated with the motions of highly compressible shearing vortices via a two-dimensional Direction Numerical Simulation (DNS). The liquid fuel is chosen as n-decane ($C_{10}H_{22}$), which is a promising surrogate fuel for a scramjet engine study, because its physicochemical properties are similar to those of practical jet fuels. A single evaporating droplet is modeled as a sub-grid point mass and tracked individually by means of the Lagrangian trajectory method. Interphase interactions including mass, momentum, and energy between the dispersed fuel droplets and the local carrier gas are modeled as source terms on the Eulerian gas-phase.

2. Numerical models

2.1. Governing equations for the gas-phase

In the present study, the motion of evaporating fuel droplets in supersonic flows[14,15] is considered, and the governing equations of the gaseous flow, including the conservations of mass, momentum, energy as well as species transportation, supplemented by the ideal gas equation of state with multiple species, are given as

$$\frac{\partial \rho}{\partial t}+\frac{\partial}{\partial x_j}(\rho u_j)=S_{\mathrm{m}} \tag{1}$$

$$\frac{\partial}{\partial t}(\rho u_i)+\frac{\partial}{\partial x_j}\left(\rho u_i u_j+P\delta_{ij}-\tau_{ij}\right)=S_{\mathrm{F},i} \tag{2}$$

$$\frac{\partial}{\partial t}(\rho e_{\mathrm{t}})+\frac{\partial}{\partial x_j}\left[(\rho e_{\mathrm{t}}+P)u_j-u_i\tau_{ij}-q_j\right]=S_{\mathrm{Q}} \tag{3}$$

$$\frac{\partial}{\partial t}(\rho Y_k)+\frac{\partial}{\partial x_j}(\rho Y_k u_j)+\frac{\partial}{\partial x_j}\left[\rho Y_k\left(V_{k,j}+V_j^{\mathrm{c}}\right)\right]=S_{\mathrm{combustion},k}+S_{Y_k} \tag{4}$$

$$P=\rho RT\sum_{k=1}^{N_S}\frac{Y_k}{W_k} \tag{5}$$

where ρ is the density. u_i and u_j are the velocities in the streamwise and transverse directions, respectively. P is the static pressure of gas. δ_{ij} is the Kronecker delta function. τ_{ij} is the Newtonian viscous stress tensor. q_j is the heat flux term. $V_{k,j}$ is the diffusion velocity of species k and V_j^{c} is the correction velocity for the global mass conservation. T is the static temperature. R is the universal gas constant. Y_k and W_k are the molecule weight and the mass fraction of species k, respectively. N_S is the total number of species. e_{t} is the total energy, i.e., kinetic energy combined with internal (containing chemical) energy, and is expressed as

$$e_{\mathrm{t}}=\sum_{k=1}^{N_S}Y_k\left(\int_{T_{\mathrm{ref}}}^{T}c_{p,k}\mathrm{d}T+h_{f,k}^0\right)-\frac{P}{\rho}+\frac{u_i u_i}{2} \tag{6}$$

where $c_{p,k}$ is the specific heat at a constant pressure of species k, and $h_{f,k}^0$ is the specific chemical formation enthalpy at the reference temperature, T_{ref}. The specific heat capacity and enthalpy are computed from the fifth-order polynomials[16]. The transport properties of the gaseous mixture are obtained based on the kinetic theory[17]. The Lennard-Jones potential model is applied to compute the inter-molecular forces. The modified Eucken model is used to calculate the thermal conductivity of each species. The Chapman-Enskog theory is utilized for the dynamic viscosity as well as the binary diffusivity. The thermal conductivity λ and the dynamic viscosity μ of the gaseous mixture are obtained from the semi-empirical mixing rule proposed by Wake and Wassiljewa.

The source terms, i.e., S_{m}, S_{F}, and S_{Q}, on the right-hand sides of the above governing equations of the gas-phase model are the interphase interaction of mass, momentum, and energy, respectively. $S_{\mathrm{combustion},k}$ is the source term, resulting from the combustion reaction. Based on the assumption of the Point-Source In Cell (PSIC) model[18], these source terms are

computed by counting the total number of droplets, N_c, in each computation cell, denoted as

$$S_m = -\frac{1}{\Delta V}\sum_{N_c}\dot{m}_d \tag{7}$$

$$S_F = -\frac{1}{\Delta V}\sum_{N_c}(F_d + \dot{m}_d u_{d,i}) \tag{8}$$

$$S_Q = -\frac{1}{\Delta V}\sum_{N_c}\left[Q_d + \dot{m}_d\left(\frac{u_{d,i}u_{d,i}}{2} + h_{V,sf}\right)\right] \tag{9}$$

$$S_{Y_k} = \begin{cases} -\frac{1}{\Delta V}\sum_{N_c}\dot{m}_d & \text{for fuel} \\ 0 & \text{for other species} \end{cases} \tag{10}$$

where ΔV is the grid size for the gas-phase. m_d is the droplet mass, and $\dot{m}_d$ represents dm_d/dt. $u_{d,i}$ is the droplet velocity. F_d and Q_d are the drag force and the convective heat transfer, respectively, which will be described later. $h_{V,sf}$ is the vapor enthalpy at the droplet surface. The source term, $S_{combustion,\ k}$, is calculated by using the chemical reaction rate per unit volume, R_F, shown as

$$S_{combustion,k} = -\frac{n_k}{n_F}\cdot\frac{W_k}{W_F}R_F \tag{11}$$

where n_F and n_k are the molar stoichiometric coefficients of the fuel and the kth species, respectively. W_F is the molecular weight of the n-decane fuel.

2.2. Governing equations for the droplet-phase

The trajectory of an evaporation spherical fuel droplet in a gaseous flow is usually tracked using the Lagrangian model. Recently, the model of a small rigid sphere in an incompressible flow[19] has been extended to compressible flows[20]. Because the density of liquid fuel is much higher than the gas density and the droplet size is sufficiently small, the unsteady force can be neglected compared to the drag force, which acts on droplets[21]. Sprayed droplets are sparsely dispersed in the present research; hence, droplet-droplet interactions are neglected. The temperature distribution inside a droplet is assumed to be uniform.

Under the above assumptions, the governing equations of a droplet for the spatial position (in the ith direction), $x_{d,i}$, velocity (in the ith direction), $u_{d,i}$, temperature, T_d, and mass, m_d, are given as follows:

$$\frac{dx_{d,i}}{dt} = u_{d,i} \tag{12}$$

$$\frac{du_{d,i}}{dt} = \frac{F_d}{m_d} = \frac{f_1}{\tau_a}(u_i - u_{d,i}) \tag{13}$$

$$\frac{dT_d}{dt} = \frac{Q_d + \dot{m}_d L_V}{m_d c_L} = \frac{f_2}{\tau_a}\cdot\frac{Nu}{3Pr}\cdot\frac{c_p}{c_L}(T - T_d) + \frac{\dot{m}_d}{m_d}\cdot\frac{L_V}{c_L} \tag{14}$$

$$\frac{dm_d}{dt} = \dot{m}_d = -m_d\frac{1}{\tau_a}\cdot\frac{Sh}{3Sc}\ln(1 + B_M) \tag{15}$$

where u_i and T are the velocity and temperature of the gas-phase seen by the droplet at its position, respectively. c_p is the specific heat of the mixture gas surrounding the droplet, and c_L is the specific heat of the liquid fuel. The droplet acceleration time, τ_a, is represented as

$$\tau_a = \frac{\rho_d d_d^2}{18\mu} \tag{16}$$

where d_d is the droplet diameter. The Prandtl and Schmidt numbers of the gas-phase are expressed as $Pr = \mu c_p/\lambda$ and $Sc = \mu/\rho D$, respectively. Here D is the mass diffusion coefficient of gas mixture. Based on the Ranz-Marshall correlations, the Nusselt and Sherwood numbers are given by

$$Nu = 2 + 0.552Re_d^{1/2}Pr^{1/3} \tag{17a}$$

$$Sh = 2 + 0.552Re_d^{1/2}Sc^{1/3} \tag{17b}$$

Here, the droplet Reynolds number, Re_d, based on the slip velocity between the local gas and the droplet, is defined as $Re_d = \rho|u_i - u_{d,i}|d_d/\mu$. f_1 is a correction[22] to the Stokes drag and is suitable for a large range of droplet Reynolds numbers in supersonic flows, which is given as

$$f_1 = \frac{Re_d}{24}\left[\frac{24}{Re_d}\left(1 + 0.15Re_d^{0.687}\right) + \frac{0.42}{1 + 42500Re_d^{-1.16}}\right] \tag{18}$$

f_2 is a correction of heat transfer for the effect of droplet evaporation and is given as $f_2 = \beta/(e^\beta - 1)$, where $\beta = -1.5Pr\tau_a(dm_d/dt)/m_d$. A Langmuir-Knudsen model considering the non-equilibrium effects on evaporation[23] is utilized. The mass transfer number, B_M, is calculated as $B_M = (Y_{sf} - Y_V)/(1 - Y_{sf})$, where Y_V is the mass fraction of fuel vapor under the far-field condition, Y_{sf} is the mass fraction of fuel vapor at the droplet surface obtained from the surface molar fraction χ_{sf}, and L_V is the latent heat of evaporation at the droplet temperature T_d.

2.3. Numerical methods

The governing equations of the present multiphase reacting flows are solved via using the in-house numerical simulation codes[14]. An overview of the numerical procedures is shown below. A finite difference methodology is utilized for solving the partial differential equations of the gas-phase. An explicit third-order Runge-Kutta scheme is applied for the time integration. The Roe-averaged matrix for the flux projection is calculated[24] for the multi-species. For the scalar conservation, a high-order accurate Maximum-Principle (MP) satisfying scheme[25] is applied. A sixth-order symmetric compact difference scheme is used to solve diffusion fluxes, and the discretization of convection fluxes is implemented by using the adaptive Central-Upwind Sixth-order Weighted Essentially Non-Oscillatory (WENO-CU6) scheme[26] to achieve a good resolution of flow properties around the shock waves in supersonic flows and to consider the low dissipation for simulating turbulent fields.

In the forward coupling (gas-to-droplet coupling), the physical quantities (velocity, temperature, pressure, viscosity and so on) of the gas-phase at the droplet center are calculated by using a fourth-order Lagrangian polynomial interpolation method. A third-order Adams-Bashforth scheme is used for the time integration of the ordinary differential equation of the droplet-phase. In the backward coupling (droplet-to-gas coupling), the PSIC model is used.

The numerical simulation codes have been previously utilized for a variety of compressible flows and combustion problems, and a series of validation studies has also been conducted[14]. The codes have been validated for non-reacting supersonic shear flow and single-droplet evaporation, and computational results are in good agreement with available experimental measurements[14].

3. Numerical set-ups

3.1. Computational domain

A spatially-developing two-dimensional shear layer is studied in the present work, as given in Fig. 1. The mixing layer is formed between a high-speed air stream with a velocity, U_{A1}, and a low-speed air stream with a velocity, U_{A2}. In Fig. 1, letters x and y represent the streamwise and transverse directions, respectively. $\delta(x)$ is the shear layer thickness at streamwise position x, and δ_0 is the initial shear layer thickness. Liquid n-decane droplets are injected into the hot-air stream from the transverse centerline, with a width of $10\delta_0$. Black dots refer to dispersed fuel droplets, and grey dots indicate droplets that are evaporating. Dash-dot lines represent large-scale vortices formed in the mixing layer, and dashed lines scale the edges of the mixing layer.

The fine-grid rectangle computational domain for the present investigation extends from $-L_y/2$ to $L_y/2$ in the transverse direction and from 0 to L_x in the streamwise direction. By setting $L_x = 4L_y$, the transverse boundaries have slight effects on the main flow in the center of the mixing layer, as well as the dynamics of the flame kernel formed in the reactive multiphase flows. The computation domain is discretized by inhomogeneous Cartesian grids, and a fine resolution is set around the center of the mixing layer. There are 512 cells and 256 cells in the streamwise and transverse directions respectively after a grid independence test.

For the inflow boundary, the distribution of the streamwise velocity is given as a hyperbolic tangent profile by using a supersonic inlet boundary condition. To excite the flow instability in the highly compressible shear layers, random disturbances are added to the transverse velocity of inflow based on the most unstable frequency of the main flow field. Non-reflective boundaries are imposed for the upper and lower boundaries since the pressure waves formed in the combustion are undesirable to reflect from the boundaries to influence the main flows. A supersonic outflow condition is utilized to set the outflow boundary.

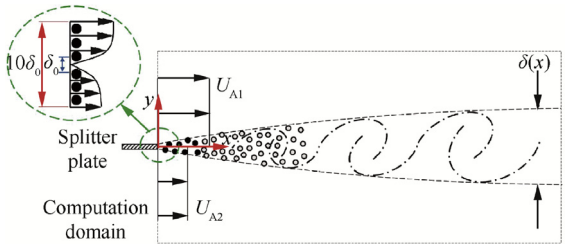

Fig. 1 Schematic of fuel spray in two-dimensional shear layer.

3.2. Inflow conditions

In this study, air is injected from the inlet boundary. We consider the inflow air as a mixture of nitrogen (N_2) and oxygen (O_2) with (in terms of mass fraction) $Y_{N_2} = 0.77$ and $Y_{O_2} = 0.23$. The temperature of the inflow air, T_0, is 1500 K. The streamwise velocity of the low-speed stream, U_{A2}, is 1242 m/s, and the velocity ratio, $U_{A1}/U_{A2} = 2$. The convective Mach number M_c for the inflow, based on the streamwise velocity difference, ΔU_A, as well as the sound velocities of the two streams, is 0.8. Spray spherical droplets injected from the inlet have the same diameter, and the injecting velocity of each droplet equals to the velocity of the local air around the droplet. The initial temperature of cold droplets is 298.15 K.

Simulation cases are summarized in Table 1, which lists the initial gaseous pressure, P_0, the inflow Reynolds number, Re_0, the initial droplet Stokes number, St_0, and the spray equivalence ratio, Φ_0. Here the subscript A means values of the airflow. $\dot{m}_{spray}$ and $\dot{m}_{air}$ are mass flow rates of spray fuel and air, respectively, and $(F/O)_{st}$ is the stoichiometric fuel to air ratio. The following conventions are applied for naming the present simulation cases: Case LP = low initial pressure, Case MP = medium initial pressure, and Case HP = high initial pressure. Initial pressures increasing from 0.1 to 0.5 MPa are utilized to study the effects of elevated pressures on ignition and combustion. The spray equivalence ratio is 1.2 for the three simulations. Note that the localized reactive mixture could be either lean or rich due to the unsteady dispersion of fuel droplets as the discrete fuel evaporating sources. Moreover, an unladen gaseous flow case with a low initial pressure, i.e., Case Unladen, is performed as a comparison.

A one-step irreversible reaction of n-decane with oxygen[27] is applied for the present study. In this chemical model, the oxidation reaction is given as

$$C_{10}H_{22} + n_{O_2}O_2 \Rightarrow n_{CO_2}CO_2 + n_{H_2O}H_2O \tag{19}$$

where n_i is the molar stoichiometric coefficient of each chemical species. The global combustion reaction constant, k (mol/(cm^3·s)), is calculated as follows:

$$k = AT^n \exp\left(-\frac{E}{RT}\right)\left(\frac{\rho Y_F}{W_F \times 10^6}\right)^a \left(\frac{\rho Y_{O_2}}{W_{O_2} \times 10^6}\right)^b \tag{20}$$

where A is the frequency factor, and E is the activation energy. Their values as well as the descriptions of n, a, and b can be found in Ref.[27]. The oxidation reaction rate per unit volume (g/(cm^3·s)) is given by $R_F = W_V k \times 10^3$.

The one-step reaction mode has been suitably used to investigate the auto-ignition of a turbulent mixture[28] and

Table 1 Summary of simulation cases.

Parameter	Case LP	Case MP	Case HP
P_0 (MPa)	0.1	0.3	0.5
$Re_0 = \frac{\rho_A \lvert U_{A1} - U_{A2} \rvert \delta_0}{\mu_A}$	1020	3060	5100
$St_0 = \frac{\tau_a}{\tau_{flow}} = \left(\frac{\rho_d d_{d,0}^2}{18\mu_A}\right) / \left(\frac{\delta_0}{\lvert U_{A1} - U_{A2} \rvert}\right)$	40	40	40
$\Phi_0 = \frac{\dot{m}_{spray}/(\dot{m}_{air} Y_{O_2})}{(F/O)_{st}}$	1.2	1.2	1.2

detonation dynamics[29] in previous research. Moreover, experiments of a shock tube[30–32] have indicated that the chemical reaction of n-decane from low to intermediate initial temperatures (< 1000 K) experiences a region of a Negative Temperature Coefficient (NTC), in which the ignition delay increases with an increase of the initial temperature, as shown in Fig. 2(a). Here Φ is the equivalence ratio and 1 atm = 1.013×10^5 Pa. When the initial temperature increases to be higher than 1000 K, the ignition delay is found to decrease linearly with an increase of the initial temperature. The single-step combustion model could exhibit this dependence of ignition delay times on the initial temperature. For the ignition of n-decane at normal pressures (0.1 MPa)[30], several experiments have shown that there seems no obvious NTC region during the ignition, and the ignition delay time has a linear inverse dependence on the initial temperature, as depicted in Fig. 2 (b). In general, the chemical reaction during the auto-ignition in a high-temperature environment has a much stronger temperature dependence than that of reactant-concentration. Therefore, the present study is limited to the simplified chemistry model, but aims to illustrate the ignition behaviors associated with motions of shearing vortices, yielding to the thermal auto-ignition and combustion converged to a high temperature of air inflows. Referred to the practical operation of a scramjet combustor, the air temperature compressed by intakes of an aircraft ranges from 1200 to 1600 K at the combustor inlet. In the present study, the inflow temperature of air streams is hence specified as 1500 K.

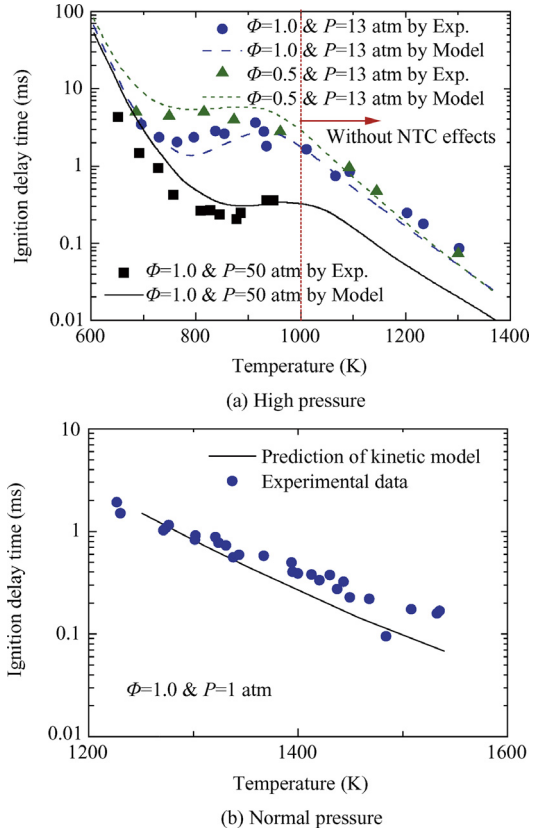

Fig. 2 Redrawn of n-decane ignition delay times in Ref.[30].

4. Results and discussions

4.1. Overall characteristics

In this section, simulation results for the whole combustion field are outlined for a later analysis of spray flame dynamics; the focus is on overall quantities that indicate compressibility, reacting flow field, and time-averaged behavior.

Fig. 3 indicates the overall features of spray combustion fields, which present the spatial distributions of instantaneous fuel droplets and the dimensionless gaseous temperature and mass fraction of fuel vapor for Case LP, Case MP, and Case HP at the same instant. Here, the grey dots indicate fuel droplets. The dispersion of fuel droplets in the upstream flow field expands transversely according to the inflow disturbance. It can be found that the dispersing droplets disappear in the downstream region prior to the roll-up of large eddies caused by droplet evaporation. Therefore, the distribution of fuel vapors is associated with the motions of eddies. The regime of the fuel vapor distribution corresponds to the pattern of large eddies, and the fuel mass accumulates in the cores of those shearing vortices. For Case LP with a normal ambient pressure, a flame firstly occurs in the high-strain vortex-braid regions, and the fuel-oxygen mixtures entrained in the large eddies are not ignited within the present computational domain due to the low gaseous temperature and pressure in the vortex cores, affected by the high compressibility. Here, it is regarded as successful ignition if continuous stable spatial combustion occurs. An increase of the ambient pressure accelerates the chemical reaction rates, and ignition occurs upstream obviously for Case MP and Case HP. For Case HP, the fuel vapors in the convective vortices are completely

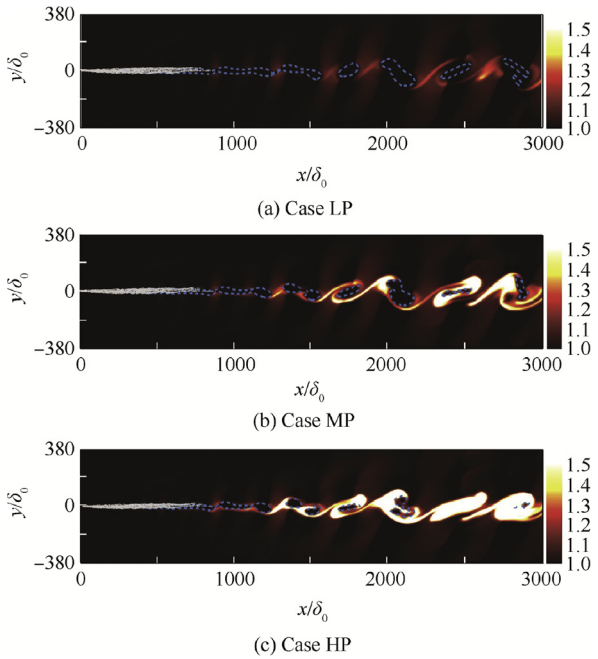

Fig. 3 Instantaneous distributions of dimensionless temperature T/T_0 and fuel mass fraction, with blue dashed lines given by $Y_F = 0.05$.

burned due to high oxidization rates, resulting in a stable flame formed in the shearing large eddies.

Fig. 4 gives the instantaneous scatter plots of the dimensionless gaseous temperature against mixture fractions. Here, a description of the combustion structure is obtained by drawing all the data in the computation domain. Here, the definition of the mixture fraction, Z, is based on the mass fractions of the gas-phase as

$$Z = \frac{Y_F - Y_O/s + Y_{O,i}/s}{Y_{F,i} + Y_{O,i}/s} \tag{21}$$

where the subscript i represents the inlet values, and s is the stoichiometric mass of oxidizer per unit mass of fuel. For the n-decane fuel in the present study, the values are $Y_{F,i} = 1.0$, $Y_{O,i} = 0.23$, and $s = 3.49$, and the value for the stoichiometric mixture fraction, $Z_{st} = 0.0618$. Moreover, the dashed lines refer to the theoretic adiabatic flame temperature against the mixture fraction.

It is found that the gaseous temperature for Case HP is generally higher than those for Case MP and Case LP at a fixed Z, especially for rich mixtures. For Case LP, the peak values of the gaseous temperature lie in the fuel-lean mixtures; it can be found in Fig. 3(a) that only the fuel-oxidizer mixtures in the high-strain vortex-braid regions are burned in a narrow flame strained between the vortices. Fig. 4(a) also shows that the temperature of fuel-rich mixtures is lower than the ambient gaseous temperature, because plenty of the fuel mass entrained in the large eddies cools the local gas, and the heat release from the chemical reaction cannot counterbalance the heat loss due to droplet evaporation. Comparisons between the scatter plots display that an increment of the ambient pressure shifts the peaks of the flame temperature from fuel-lean to stoichiometric conditions, since a pressure increase results in an acceleration of the exothermic reaction rate.

Followed by the above demonstrations of the instantaneous characteristics of the overall reacting flow field, the below discussion will display time-averaged features. Comparisons of the streamwise distributions of the time-averaged gaseous temperature, $\bar{T}$, as well as standard deviations of temperature, σ_T, at $y = 0.5L_y$, are shown in Fig. 5. σ_T denotes the intensity of temperature perturbation. These first- and second-order statistics are normalized by the initial gaseous temperature, T_0. Compared with the unladen flow, the streamwise variations of $\bar{T}$ for the droplet-laden cases display a decrease upstream due to the cooling effects from the evaporation of fuel spray droplets. After ignition occurs, the heat release from the exothermic reaction increases the gaseous temperature. It is observed that the values of $\bar{T}$ for Case HP are higher than those of the other cases with lower ambient pressures. However, the streamwise variations of σ_T show that the temperature fluctuations for Case HP are found to be much higher than those of the other cases; the discrepancy becomes marked downstream after the ignition occurs. During the droplet evaporation process, before an ignition kernel is established, the high values of σ_T for Case HP are mainly attributed to the high turbulence intensities associated with high Reynolds numbers. After the exothermic chemical reaction starts to consume the fuel vapors, the increasing temperature from the chemical heat

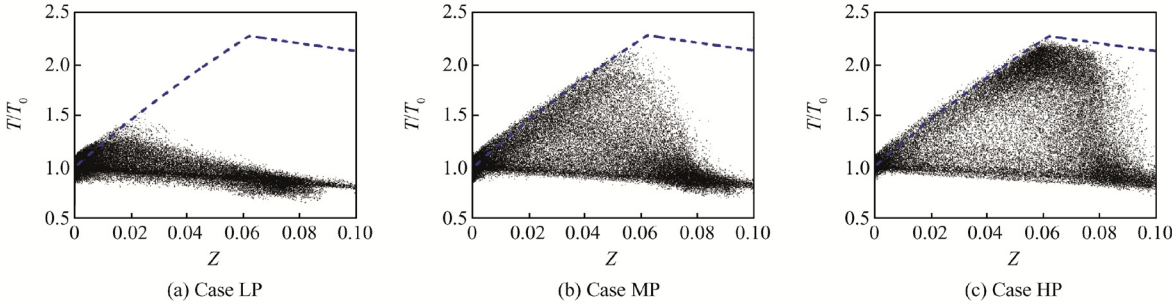

(a) Case LP (b) Case MP (c) Case HP

Fig. 4 Scatter plots of instantaneous dimensionless temperature T/T_0 vs mixture fraction Z.

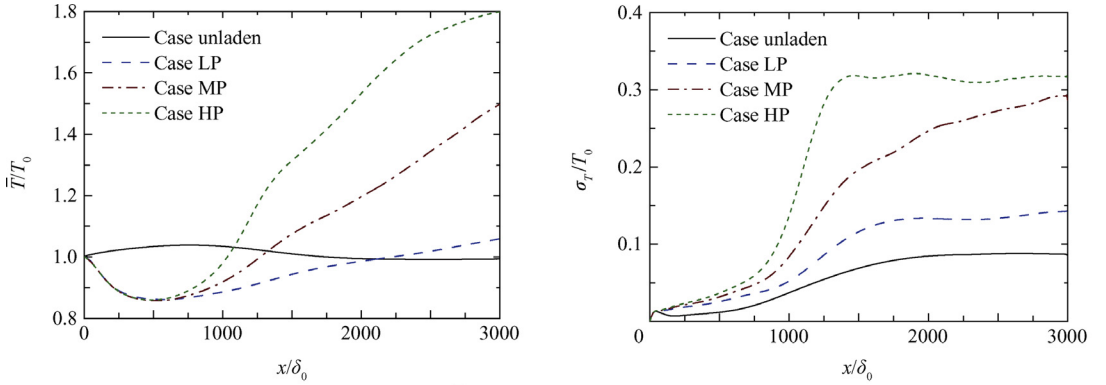

(a) Dimensionless time-averaged temperature $\bar{T}/T_0$ (b) Dimensionless standard deviations of temperature σ_T/T_0

Fig. 5 Spatial variations of values along streamwise direction at $y = 0.5L_y$.

release enlarges the temperature fluctuations, resulting in an increase of σ_T. Moreover, the elevated pressures accelerate the chemical reactions and enhance the combustion, which lead to a high temperature and large temperature fluctuations.

The mixing layer thickness provides a length scale for the development of the mixing region and shows self-similarity characteristics. The streamwise evolution of the mixing layer thickness, δ, for the cases considered is shown in Fig. 6. For Case Unladen, after a transient of the roll-up of eddies, a quasi-linear growth regime of δ is found, and the mixing layer becomes self-similar. From a comparison between Case LP and Case Unladen, it is observed that the modulation from evaporating fuel droplets accelerates the development of the mixing layer, and the droplet-laden flows achieve a linear growth of δ at an upper streamwise location. With an increment of the ambient pressure, the growth rate of the mixing layer thickness, $\mathrm{d}\delta/\mathrm{d}x$, tends to be high. This is because turbulence becomes strong as the density (i.e., the Reynolds number) increases. The streamwise location of ignition is marked in Fig. 6. It is found that downstream combustion decreases the growth rate of δ, and the reduction of the growth rate becomes obvious with increasing pressures associated with enhanced combustion. The thickness of the mixing layer, δ, grows more slowly for the reacting cases than that for the inert case, which agrees with earlier research results of compressible flows with small convective Mach numbers[33]. The differences come from the effects of the decrease in Reynolds stresses due to the heat release from the exothermic reaction in reacting flows.

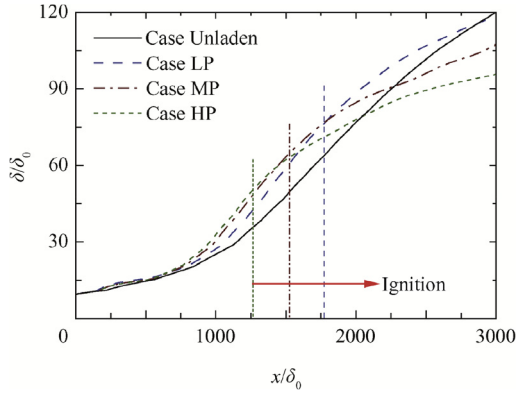

Fig. 6 Spatial variations of mixing layer thickness for unladen and laden simulations.

4.2. Instantaneous features

In this section, the ignition and dynamics of a spray flame with elevated pressures are investigated by analyzing the time-series data of the combustion field and by tracking the evolution of flame kernels with the turbulent motions of large eddies.

For evaluating the effects of elevated pressures on the instantaneous features of ignition as well as combustion, we record the maximum values of the fuel mass fraction and chemical reaction rate in the flow-field during one flow circle, since droplets are injected into the carrier flow, as depicted in Fig. 7. Here, the dimensionless time is $t^* = t/t_{\mathrm{flow}}$, in which t_{flow} is the characteristic time of a flow circle. Cold fuel droplets enter the hot gaseous flow and evaporate, resulting in a fast increase of fuel vapors in the flow field. At the initial increase stage of $Y_{\mathrm{F,\,max}}$, the effects of elevated pressures are not obvious. However, after time $t^* = 0.1$, an increase of the ambient pressure results in an increase of the growth rate of $Y_{\mathrm{F,\,max}}$. Although the differences between the three cases are slight, the effects on the chemical reaction rates are found to be significant. As the fuel droplets evaporate to form vapors, a pressure rise obviously accelerates the chemical reactions.

The maximum gaseous temperature in the combustion field during five flow circles once fuel droplets are injected into the carrier flow are then recorded, as shown in Fig. 8(a). It is found that the maximum gaseous temperature is enlarged by a factor of 1.1 compared with the initial gaseous temperature T_0 before the injection of fuel droplets. This is because that the high compressibility effect leads to a partial recovery of the kinetic energy of the free-stream, as discussed before. The distinction between the burning and non-burning conditions is arbitrarily specified at a temperature of $T_{\mathrm{ig}} = T_0 + \Delta T$ ($=500$ K). The initial droplet mass flow rate is the same for all three simulations, but the times of occurrence of flame kernels decrease as the ambient pressure increases. This is attributed to the fact that an increase of the ambient pressure accelerates the chemical reaction rate. For Case LP, judging from the time-series T^*_{max}, extinction occurs in the flow field, and a less stable combustion mode appears, compared with the high-pressure

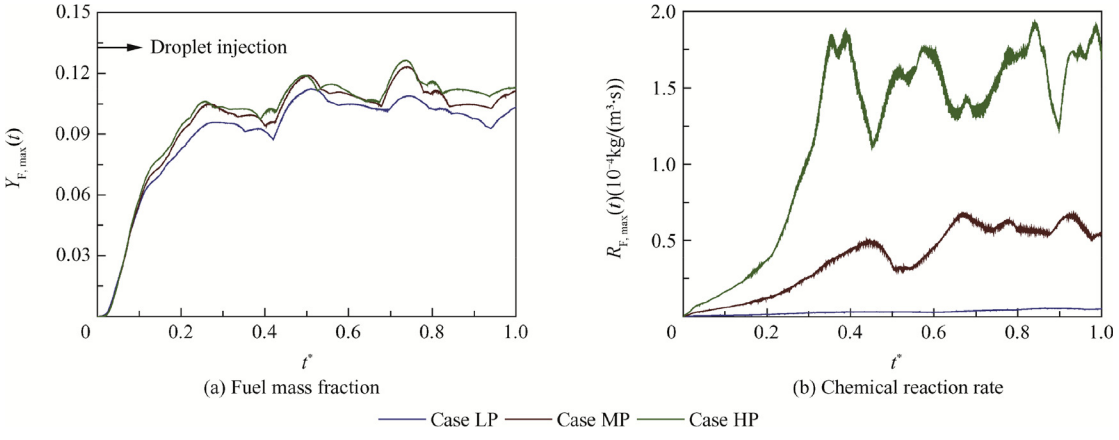

Fig. 7 Maximum values in flow-field during one flow circle since droplets are injected.

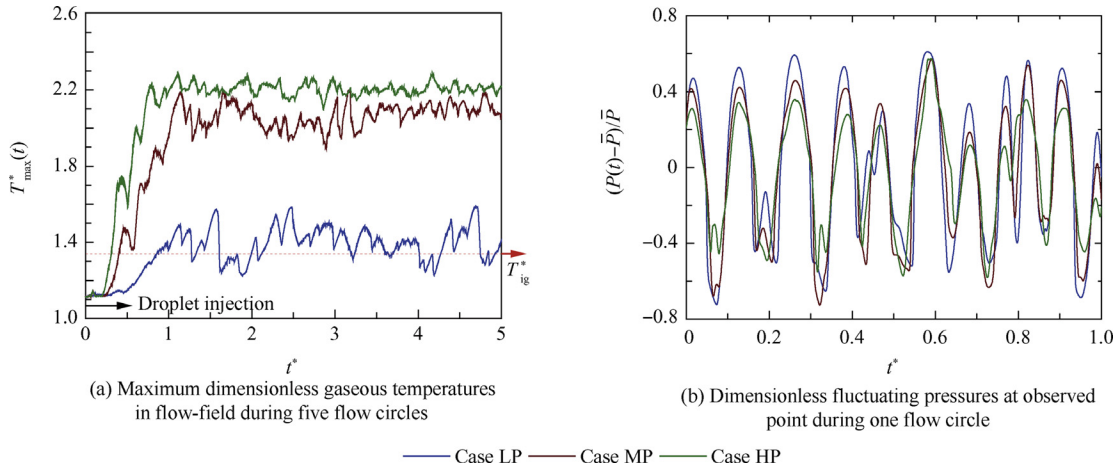

Fig. 8 Variations of temperature and pressure in flow field.

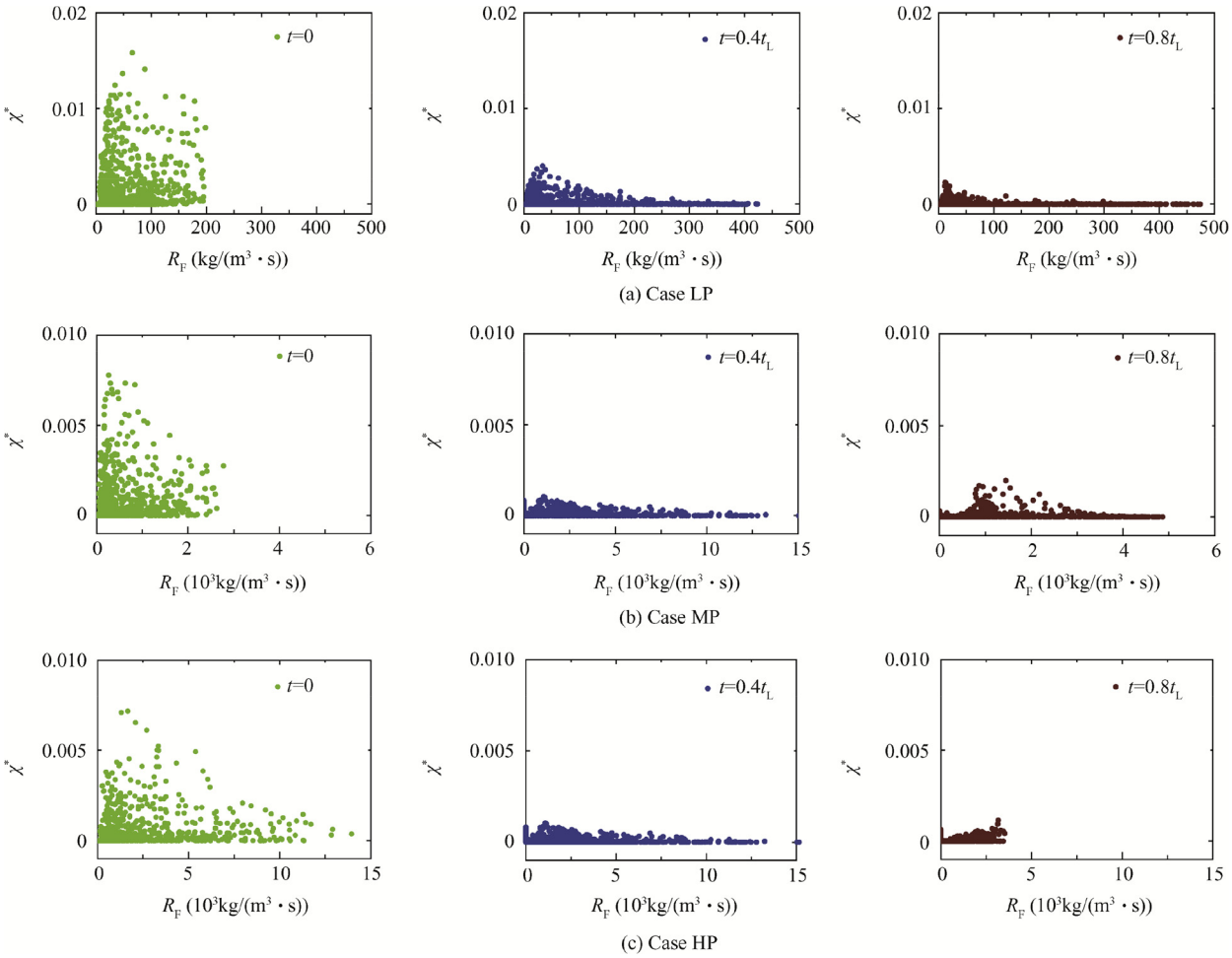

Fig. 9 Scatter plots of dimensionless scalar dissipation rate vs chemical reaction rate at times $t = 0$, $t = 0.4t_L$, and $t = 0.8t_L$.

cases. Fig. 8(b) shows the time evolutions of dimensionless fluctuating pressures for all three cases at an observed point ($x/\delta_0 = 2000$, $y/\delta_0 = 0$) in the combustion field. Pressure fluctuations are obtained based on the time-averaged pressure, $\bar{P}$, at the observed point. It is found that pressure oscillations display synthesized-sinusoidal shapes for all simulations. Shearing vortices move coherently in the mixing layer. Low and high pressures appear at the centers of the vortexes and the strain regions between the vortices, respectively. Therefore, such a sinusoidal shape of pressure fluctuations caused by the

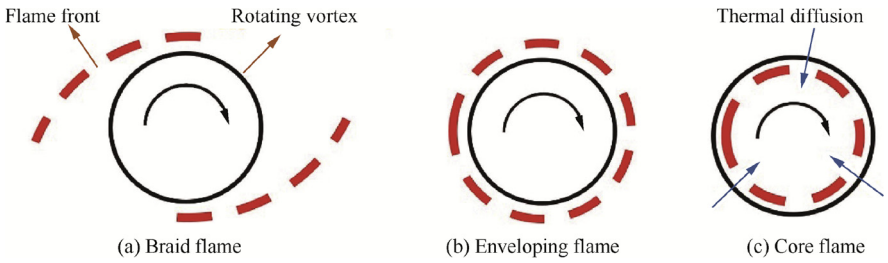

Fig. 10 Schematic diagram of evolution of a spray flame in shearing vortex.

periodic motions of coherent structures in the flow field could be observed at a fixed Eulerian point. Obviously, a high ambient pressure could lead to a large fluctuation amplitude, because the pressure undergoes strong oscillations during the turnover of vortices. Here, we normalize the pressure fluctuations to eliminate the effects of vortex dynamics; hence, we could focus on the influence of an elevated pressure on the combustion and further the pressure oscillations. It is observed that a disparity of pressure fluctuations among the three cases can be observed in the peak values of pressure, where the peaks are smoother with an increasing ambient pressure. As observed in Fig. 3(a) for Case LP, a flame only occurs in the vortex-braid regions, which means that the combustion is spatially intermittent. Therefore, the unstable combustion results in relatively large oscillations of temperature and pressure. For Case HP, flame kernels are formed not only in the vortex-braids but also in the vortex-cores, and the more stable combustion leads to a reduction of the fluctuating pressures.

Fig. 9 depicts the scatter plots of the dimensionless scalar dissipation rate, χ^*, versus the chemical reaction rate, R_F, for a shearing vortex at instant times $t = 0$, $t = 0.4t_L$, and $t = 0.8t_L$. t_L is the time when the vortex completes an eddy turnover. The data is sampled at the computation grids in the domain for the vortex. The scalar dissipation rate, χ, is defined as

$$\chi = 2D_F|\nabla Z|^2 \tag{22}$$

where D_F is the mass diffusion coefficient of fuel in the gas mixture. χ^* of the mixture fraction is normalized by $\chi^* = \chi/(|U_{A1} - U_{A2}|/\delta_0)$. For the three cases, it is found that incipient reaction spots originate in regions with high scalar dissipation rates at time $t = 0$, corresponding to the high-strain vortex-braid zones with high temperatures and pressures. Moreover, χ^* for Case HP and Case MP are slower than that of Case LP. This is because the fast chemical reactions for Case HP and Case MP consume the local fuel-oxygen mixtures in a short time, resulting in a decrease of the local mixture gradient. Another reason is that the higher turbulence for Case HP and Case MP promotes scalar mixing. Subsequently, for the three cases, reaction spots form in the regions with a quite lower χ^* at time $t = 0.4t_L$. The reason for this phenomenon is that the merging of two neighbor vortices contributes to the mixing of scalars, as well as the dissipation. For Case LP, the local flammable mixtures in the vortex-braids are burned continuously from $t = 0.4t_L$ to $t = 0.8t_L$ due to the self-acceleration of the combustion rate. Therefore, the local gradient of scalars is dissipated, and χ^* is reduced. At time $t = 0.8t_L$, for Case HP, the reactants within the vortex are burned, and the chemical reaction rates decrease due to a lack of flammable mixtures. It is also found that the most reactive spots localize in regions with low dissipation rates.

The evolution of the spray flame in highly compressible shearing vortices can be summarized as three stages; the scenarios are depicted in Fig. 10, in which the black circle means a rotating vortex entraining fuel-oxygen mixtures, and the arrow refers to the rotating direction. Flame fronts are sketched using red dashed lines. At first, an ignition kernel occurs at the braid structures due to the local high temperatures and pressures of the gas-phase, as shown by Fig. 10(a), and braid flames are formed. Then, the flame propagates to envelop the vortex associated with the rotation process, and reactive pockets in the periphery of the vortex burn with enveloping flames (see Fig. 10(b)). Subsequently, thermal diffusion from the periphery of the vortex heats the inner fuel–air mixtures, as shown by the blue arrows in Fig. 10(c), and combustion finally occurs in the rich mixtures within the vortex core, resulting in a core flame.

5. Conclusions and remarks

The present paper numerically investigates the overall behavior and instantaneous characteristics of spray flames in highly compressible vortices formed in shearing flows laden with n-decane droplets. The gas-droplet reacting flow system is numerically captured by a hybrid Eulerian-Lagrangian method, in which the dispersion of evaporating dispersed droplets is tracked in the Lagrangian frame. The high-Mach number gaseous flow is simulated by DNS in the Eulerian frame.

The overall behavior of the flow field with high convective Mach numbers shows that the high-speed flow compressibility effect is obvious. High- and low-temperature regions are interlaced, formed in vortex braids and cores, respectively. For spray flames associated with shearing vortices, ignition kernels occur at high-strain vortex braids with high scalar dissipation rates. Then, the flame kernels are strained, associated with the rotation of the vortex, and propagate to envelop the vortex. The flammable mixtures entrained in the vortex are burned from the edge to the core of the vortex until the reactants within the shearing vortex are completely consumed. With an increment of the ambient pressure, the regime with a high temperature tends to be larger, the time-averaged temperature increases, and the fluctuating pressure decreases, resulting in a more stable combustion.

The influence of initial droplet sizes as well as spray equivalence ratios on supersonic combustion characteristics in mixing layers will be studied in details in the future for better understanding the physics of compressible spray flames.

Acknowledgements

The second author would like to thank the partial finical supports from the National Natural Science Foundation of China (No. 51676111), the Joint Fund of the National Natural Science Foundation of China and the China Academy of Engineering Physics (No. U1730104), and the Tsinghua University Initiative Scientific Research Program, China (No. 2014Z05091).

References

1. Miller RS. Effects of nonreacting solid particle and liquid droplet loading on an exothermic reacting mixing layer. *Phys Fluids* 2001;**13**(11):3303–20.
2. Khatumria VC, Miller RS. Numerical simulation of a fuel droplet laden exothermic reacting mixing layer. *Int J Multiph Flow* 2003; **29**(5):771–94.
3. Reveillon J, Vervisch L. Analysis of weakly turbulent dilute-spray flames and spray combustion regimes. *J Fluid Mech* 2005;**537**:317–47.
4. Martínez-Ruiz D, Urzay J, Sánchez AL, Liñán A, Williams FA. Dynamics of thermal ignition of spray flames in mixing layers. *J Fluid Mech* 2013;**734**:387–423.
5. Russo S, Gomez A. Physical characterization of laminar spray flames in the pressure range 0.1–0.9 MPa. *Combust Flame* 2006;**145**(1):339–56.
6. Nakamura M, Nishioka D, Hayashi J, Akamatsu F. Soot formation, spray characteristics, and structure of jet spray flames under high pressure. *Combust Flame* 2011;**158**(8):1615–23.
7. Kitano T, Nakatani T, Kurose R, Komori S. Two-dimensional direct numerical simulation of spray flames—Part 2: Effects of ambient pressure and lift, and validity of flamelet model. *Fuel* 2013;**104**:526–35.
8. Kitano T, Nishio J, Kurose R, Komori S. Effects of ambient pressure, gas temperature and combustion reaction on droplet evaporation. *Combust Flame* 2014;**161**(2):551–64.
9. Nakamura M, Akamatsu F, Kurose R, Katsuki M. Combustion mechanism of liquid fuel spray in a gaseous flame. *Phys Fluids* 2005;**17**(12) 123301.
10. Fujita A, Watanabe H, Kurose R, Komori S. Two-dimensional direct numerical simulation of spray flames—Part 1: effects of equivalence ratio, fuel droplet size and radiation, and validity of flamelet model. *Fuel* 2013;**104**:515–25.
11. Kitano T, Kaneko K, Kurose R, Komori S. Large-eddy simulations of gas-and liquid-fueled combustion instabilities in back-step flows. *Combust Flame* 2016;**170**:63–78.
12. Schroll P, Wandel AP, Cant RS, Mastorakos E. Direct numerical simulations of autoignition in turbulent two-phase flows. *Proc Combust Inst* 2009;**32**(2):2275–82.
13. Wang Y, Rutland CJ. Direct numerical simulation of ignition in turbulent n-heptane liquid-fuel spray jets. *Combust Flame* 2007;**149** (4):353–65.
14. Ren Z, Wang B, Xie Q, Wang D. Thermal auto-ignition in high-speed droplet-laden mixing layers. *Fuel* 2017;**191**:176–89.
15. Ren Z, Wang B, Yang S, Xie Q, Liu H, Wang D. Evolution of flame kernel in one eddy turnover of high-speed droplet laden shear layers. *J Loss Prevent Process Indust* 2017;**49**:938–46.
16. Burcat A, Ruscic B. *Third millenium ideal gas and condensed phase thermochemical database for combustion with updates from active thermochemical tables*. Argonne: Argonne National Laboratory; 2005. p. 1–417.
17. Poling BE, Prausnitz JM, John Paul OC, Reid RC. *The properties of gases and liquids*. New York: McGraw-Hill; 2001.
18. Crowe CT, Sharma MP, Stock DE. The particle-source-in cell (PSI-CELL) model for gas-droplet flows. *J Fluids Eng* 1977; **99**(2):325–32.
19. Clift R, Grace JR, Weber ME. *Bubbles, drops, and particles*. New York: Courier Corporation; 2005. p. 97–125.
20. Parmar M, Haselbacher A, Balachandar S. Equation of motion for a sphere in non-uniform compressible flows. *J Fluid Mech* 2012;**699**: 352–75.
21. Mashayek F. Direct numerical simulations of evaporating droplet dispersion in forced low Mach number turbulence. *Int J Heat Mass Transf* 1998;**41**(17):2601–17.
22. Loth E. Compressibility and rarefaction effects on drag of a spherical particle. *AIAA J* 2008;**46**(9):2219.
23. Miller RS, Harstad K, Bellan J. Evaluation of equilibrium and non-equilibrium evaporation models for many-droplet gas-liquid flow simulations. *Int J Multiph Flow* 1998;**24**(6):1025–55.
24. Fedkiw RP, Merriman B, Osher S. High accuracy numerical methods for thermally perfect gas flows with chemistry. *J Comput Phys* 1997;**132**(2):175–90.
25. Zhang X, Shu CW. On maximum-principle-satisfying high order schemes for scalar conservation laws. *J Comput Phys* 2010;**229**(9): 3091–120.
26. Hu XY, Wang Q, Adams NA. An adaptive central-upwind weighted essentially non-oscillatory scheme. *J Comput Phys* 2010; **229**(23):8952–65.
27. Westbrook CK, Dryer FL. Chemical kinetic modeling of hydrocarbon combustion. *Prog Energy Combust Sci* 1984;**10**(1):1–57.
28. Lodier G, Merlin C, Domingo P, Vervisch L, Ravet F. Self-ignition scenarios after rapid compression of a turbulent mixture weakly-stratified in temperature. *Combust Flame* 2012;**159**(11):3358–71.
29. Verreault J, Higgins AJ, Stowe RA. Formation of transverse waves in oblique detonations. *Proc Combust Inst* 2013;**34**(2): 1913–20.
30. Gokulakrishnan P, Klassen MS, Roby RJ. Development of detailed kinetic mechanism to study low temperature ignition phenomenon of kerosene. *ASME turbo expo 2005: power for land, sea, and air*; 2005 Jun 6-9; Reno-Tahoe, USA. New York: American Society of Mechanical Engineers; 2005. p. 191–200.
31. Kumar K, Mittal G, Sung CJ. Autoignition of n-decane under elevated pressure and low-to-intermediate temperature conditions. *Combust Flame* 2009;**156**(6):1278–88.
32. Shen HPS, Steinberg J, Vanderover J, Oehlschlaeger MA. A shock tube study of the ignition of n-heptane, n-decane, n-dodecane, and n-tetradecane at elevated pressures. *Energy Fuels* 2009; **23**(5):2482–9.
33. Knaus R, Pantano C. On the effect of heat release in turbulence spectra of non-premixed reacting shear layers. *J Fluid Mech* 2009;**626**: 67–109.